

# Surface layer climate and turbulent exchange in the ablation zone of the west Greenland ice sheet

Michiel van den Broeke,\* Paul Smeets and Janneke Ettema

*Utrecht University, Institute for Marine and Atmospheric research (IMAU), 3508 TA Utrecht, The Netherlands*

**ABSTRACT:** A comprehensive description is presented of the surface layer (SL) wind, temperature and humidity climate and the resulting sensible and latent heat exchange in the ablation zone of the west Greenland ice sheet. Over a four-year period (August 2003–August 2007), data were collected using three automatic weather stations (AWS) located along the 67°N latitude circle at 6, 38 and 88 km from the ice sheet margin at elevations of 490, 1020 and 1520 m asl. In the lower ablation zone, surface momentum roughness peaks in summer, which enhances the mechanical generation of turbulence in the stable SL. The SL is stably stratified throughout the year: in summer, the surface temperature is maximised at the melting point and therefore remains colder than the overlying air, in winter the surface is cooled by a radiation deficit. The resulting downward directed sensible heat flux cools the SL air. Humidity gradients between surface and air are small in winter, in response to low temperatures, but peak in spring, when the surface is not yet melting and can freely increase its temperature. This is especially true for the lower ablation zone, where winter accumulation is small so that the dark ice surface is already exposed at the onset of spring, allowing significant convection and sublimation. During summer, when the surface is melting, the sensible heat flux becomes directed towards the surface and sublimation changes into deposition in the lower ablation zone. The SL wind climate is dominated by katabatic forcing, with high directional constancy in summer and winter. The katabatic forcing is important to maintain turbulent exchange in the stable Greenland SL. Copyright © 2008 Royal Meteorological Society

**KEY WORDS** Greenland; climate; turbulent fluxes

*Received 22 October 2008; Accepted 25 October 2008*

## 1. Introduction

With a potential sea level rise of 7 m, the Greenland ice sheet (GrIS) is the largest source of fresh water in the Northern Hemisphere (Bamber *et al.*, 2001). Recent observations suggest that the GrIS is significantly contributing to ongoing sea level rise (Cazenave, 2006; Lemke *et al.*, 2007). In spite of its importance, the GrIS mass budget is still poorly known. Mass balance models based on energy balance or degree-day considerations depend on poorly known input parameters such as clouds (for longwave radiation), solid precipitation (for mass balance and albedo) and near surface air temperature (for longwave radiation, sensible heat flux (SHF) and degree days, Bøggild *et al.*, 1994; Braithwaite, 1995; Van de Wal and Oerlemans, 1997). Moreover, these approaches do not take into account the dynamical atmospheric feedbacks that are known to exist between katabatic forcing and turbulent heat exchange under melting conditions (Oerlemans and Grisogono, 2002).

When coupled to a physical snow model, regional atmospheric climate models provide the right combination of high resolution and atmospheric/snow physics to study the present-day and future mass balance of the

GrIS (Cassano *et al.*, 2001; Dethloff *et al.*, 2002; Box *et al.*, 2006; Fettweis, 2007). Unfortunately, validation of these models suffers from a paucity of energy and mass balance observations, specifically from the GrIS ablation zone. To resolve this, automatic weather stations (AWS) are increasingly being used. In 1995, the Greenland Climate Network (GC-Net), coordinated by CIRES, started off as part of the NASA funded PARCA project. GC-Net presently consists of over 15 AWS along the 2000 m height contour as well as in the ablation zone in north and west Greenland (Steffen and Box, 2001). As a contribution to this network, UU/IMAU installed three AWS along the K-transect in the ablation zone in southwest Greenland in August 2003.

Here, we present the first four years of the wind, temperature and humidity observations from these three AWS. Analogous to the method used in atmospheric models, we use surface layer (SL) similarity theory to calculate the turbulent fluxes of sensible and latent heat from single-level AWS observations in combination with assumptions made about the state of the surface. Direct eddy correlation measurements performed at S6 are used to validate the calculations. First, we discuss the field area and instruments in Section 2, calculation methods and validation in Section 3, followed by a discussion of the results in Section 4 and summary and conclusions in Section 5.

\* Correspondence to: Michiel van den Broeke, Utrecht University, Institute for Marine and Atmospheric research (IMAU), 3508 TA Utrecht, The Netherlands. E-mail: m.r.vandenbroeke@uu.nl

## 2. Field area and instrumentation

### 2.1. Field area

The AWS are located at sites S5, S6 and S9 of the K-transect, a mass balance stake array that extends from the ice margin to 1800 m asl along the 67°N latitude circle. These sites are located at a distance of 6, 38 and 88 km from the ice sheet margin at elevations of 490, 1020 and 1520 m asl (Figure 1). This part of Greenland is characterised by a strip of tundra ~150 km wide and an ablation zone that extends ~100 km onto the ice sheet. Figure 2 shows the AWS and their surroundings in late August 2006, marking the end of the ablation season. Note that the surface at S5 is very irregular with 2–3 m high ice hills, while at S9 the surface is much smoother.

### 2.2. Automatic weather stations

The high summer melt rates do not allow for the use of masts that are rigidly fixed to the surface. The AWS structure consists of a central pole and four legs that spread out from the centre making a small angle with the surface (Figure 2). Once placed, the legs rapidly melt about 0.5 m into the ice, and are then firmly fixed to the ice surface. In the course of the ablation season the masts melt down with the ice surface and maintain their upright position within a few degrees.

The AWS measure wind speed and direction, temperature and relative humidity at approximately 2 and 6 m above the surface at the day of installation. Air pressure is measured in the electronics enclosure. The AWS are also equipped with Kipp & Zonen (K&Z) CNR1 net radiometers, results of which were reported in Van

den Broeke *et al.* (2008a). Accumulation and ablation is monitored with a sonic height ranger, which is attached to three stakes that are fixed in the ice. This enables us to reconstruct the snow depth and instrument height throughout the year (Van den Broeke *et al.*, 2008b). All variables are sampled at 6 min intervals (instantaneous, except for wind speed, cumulative) after which 1-h averages are stored in a Campbell CR10 datalogger with separate memory module. Instrument specifications are listed in Table I.

### 2.3. Eddy correlation measurements

The eddy correlation measurements at S6 have been described in detail by Smeets and Van den Broeke (2008a,b). The measurements were performed from 30 August 2003 to 18 August 2004 at an initial height of 2.75 m. Three-axial wind speeds ( $u'$ ,  $v'$ ,  $w'$ ) and virtual temperature  $T_v$  were measured using a sonic anemometer, while a thermocouple and fast hygrometer measured air temperature and specific humidity. The sensors were pointed into the prevailing wind direction. Data were sampled at 10 Hz in the so-called *single-measurement mode*, which combines minimal power requirements with the highest possible frequency response (about 60 Hz). Fluxes and variances are therefore hardly subjected to low-pass filtering but contain less samples of a high frequency signal resulting in some loss of accuracy. Every 10 min the mean, standard deviation and covariance values were calculated and stored on a Campbell CR23X datalogger. Solar cells, a wind generator and a battery pack provided the energy for the turbulence sensors.

### 2.4. AWS data treatment

Energy considerations do not allow aspiration of the AWS temperature sensors. Radiation errors in the (unventilated) air temperature measurement of up to 3 °C occurred under conditions of low wind speed and high insolation. This was successfully corrected to less than 0.5 °C by comparing AWS air temperature to one year of in situ thermocouple temperatures, which were part of the eddy correlation set-up. Snow height data at S6 were missing for the winter and spring of 2005: for this period, maximum snow height, onset of melt and timing of snow-pack disappearance were estimated using an energy balance model, and snow height was linearly interpolated in between. Relative humidity at all sites was corrected along the lines of Anderson (1994). AWS values were converted to standard heights (2 m for temperature and humidity, 10 m for wind speed) using the flux profile relations (see below).

## 3. Calculation and validation of turbulent fluxes

### 3.1. Bulk method

The turbulent fluxes of SHF and latent heat (LHF) follow from:

$$\begin{aligned} SHF &= -\rho c_p \overline{(w'\theta')} = \rho c_p u_* \theta_* \\ LHF &= -\rho L_s \overline{(w'q')} = \rho L_s u_* q_* \end{aligned} \quad (1)$$

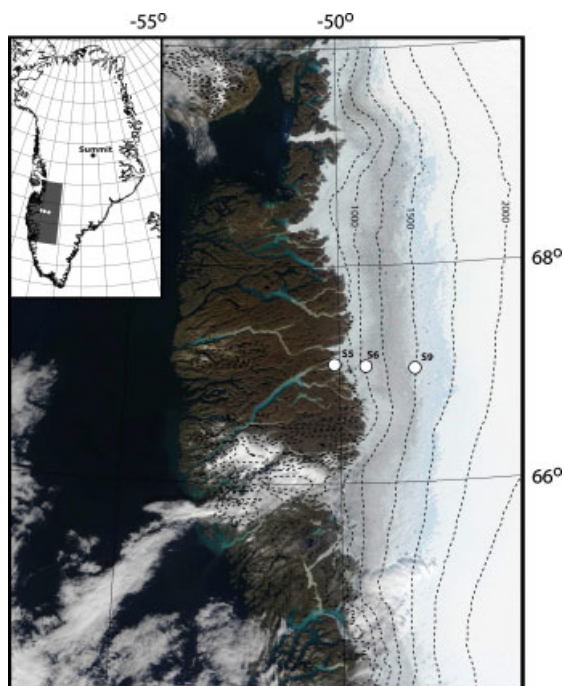


Figure 1. MODIS scene of west Greenland (August 23, 2006) with AWS locations (white dots) and ice sheet elevation contours (dashed lines, height interval 250 m, from Bamber *et al.*, 2001). This figure is available in colour online at [www.interscience.wiley.com/ijoc](http://www.interscience.wiley.com/ijoc)

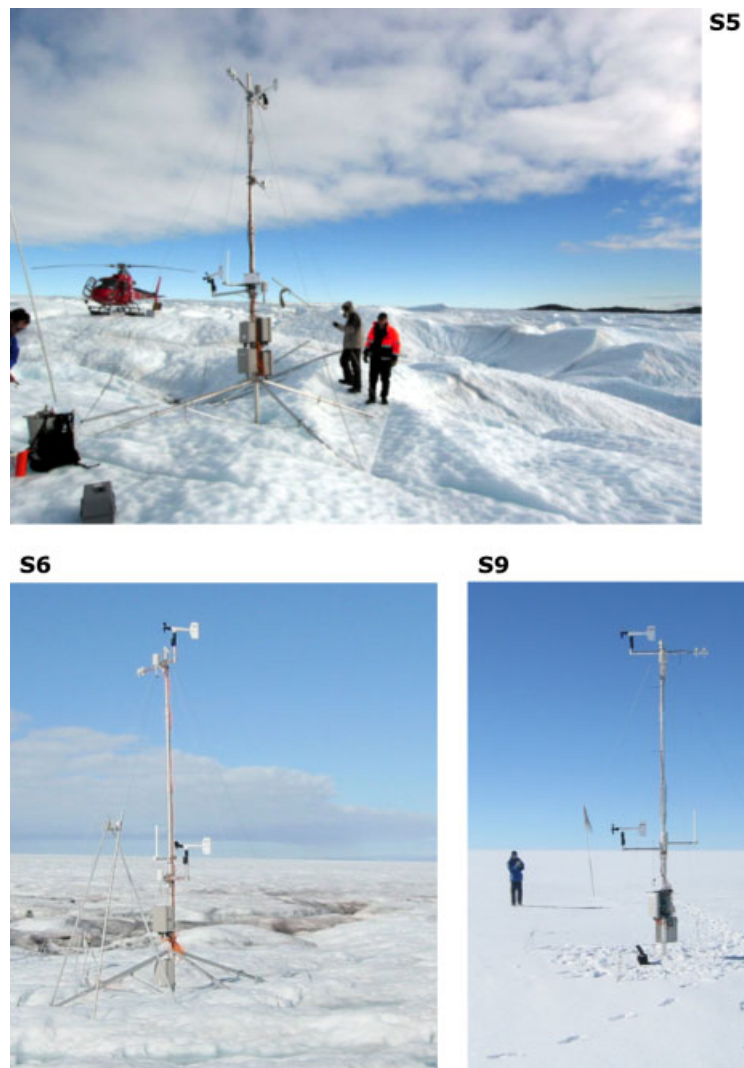


Figure 2. Images of AWS locations at S5 (August 27, 2006), S6 and S9 (both August 26, 2006). This figure is available in colour online at [www.interscience.wiley.com/ijoc](http://www.interscience.wiley.com/ijoc)

Table I. AWS and turbulence sensor specifications. EADT = Estimated Accuracy for Daily Totals.

AWS sensors	Type	Range	Accuracy
Air pressure	Vaisala PTB101B	600 to 1060 hPa	4 hPa
Air temperature	Vaisala HMP35AC	-80 to +56 °C	0.3 °C
Relative humidity	Vaisala HMP35AC	0 to 100%	2% (RH < 90%) 3% (RH > 90%)
—	—	—	—
Wind speed	Young 05103	0 to 60 m s <sup>-1</sup>	0.3 m s <sup>-1</sup>
Wind direction	Young 05103	0 to 360°	3°
Pyranometer	Kipp en Zonen CM3	305 to 2800 nm	EADT +/-10%
Pyrradiometer	Kipp en Zonen CG3	5000 to 50 000 nm	EADT +/-10%
Snow height	Campbell SR50	0.5 to 10 m	0.01 m or 0.4%
Turbulence sensors	Type	Accuracy	—
Velocity	CSAT3 Sonic Anemometer	Offset error < +/- 0.04 m s <sup>-1</sup>	—
Virtual temperature	CSAT3 Sonic Anemometer	Resolution +/-0.025 °C	—
Temperature	FW3 Type E Thermocouple	+/-0.2 °C	—
Specific humidity	LiCor LI-7500 FW3	RMS noise <0.005 g kg <sup>-1</sup>	—

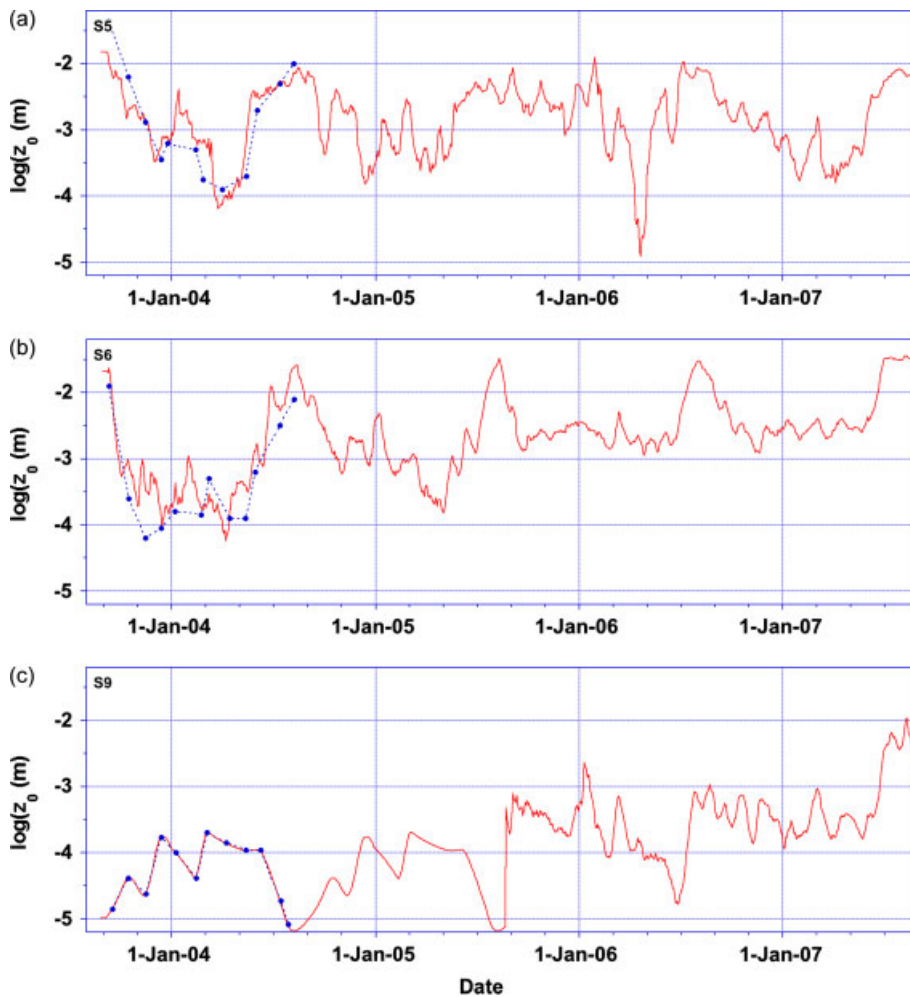


Figure 3. Twenty-day running mean surface momentum roughness  $z_{0,v}$  from two-level AWS data (red lines) and 20-day-binned values from SB08 at (a) S5, (b) S6 and (c) S9. For AWS 9, not enough reliable wind profile data were available for the first two years; instead, the SB08 data have been used. This figure is available in colour online at [www.interscience.wiley.com/ijoc](http://www.interscience.wiley.com/ijoc)

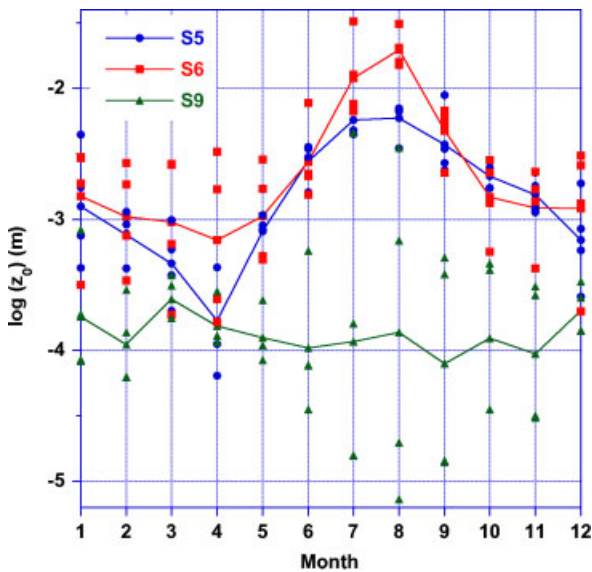


Figure 4. Average seasonal cycle, based on monthly means, of surface momentum roughness  $z_{0,v}$  (individual months indicated by symbols). This figure is available in colour online at [www.interscience.wiley.com/ijoc](http://www.interscience.wiley.com/ijoc)

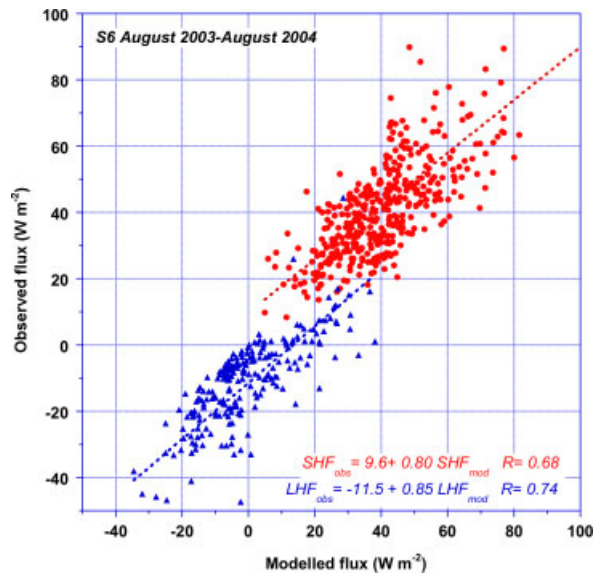


Figure 5. Comparison of modelled and directly measured hourly mean values of SHF (red dots) and LHF (blue triangles) at S6, August 2003–August 2004. This figure is available in colour online at [www.interscience.wiley.com/ijoc](http://www.interscience.wiley.com/ijoc)

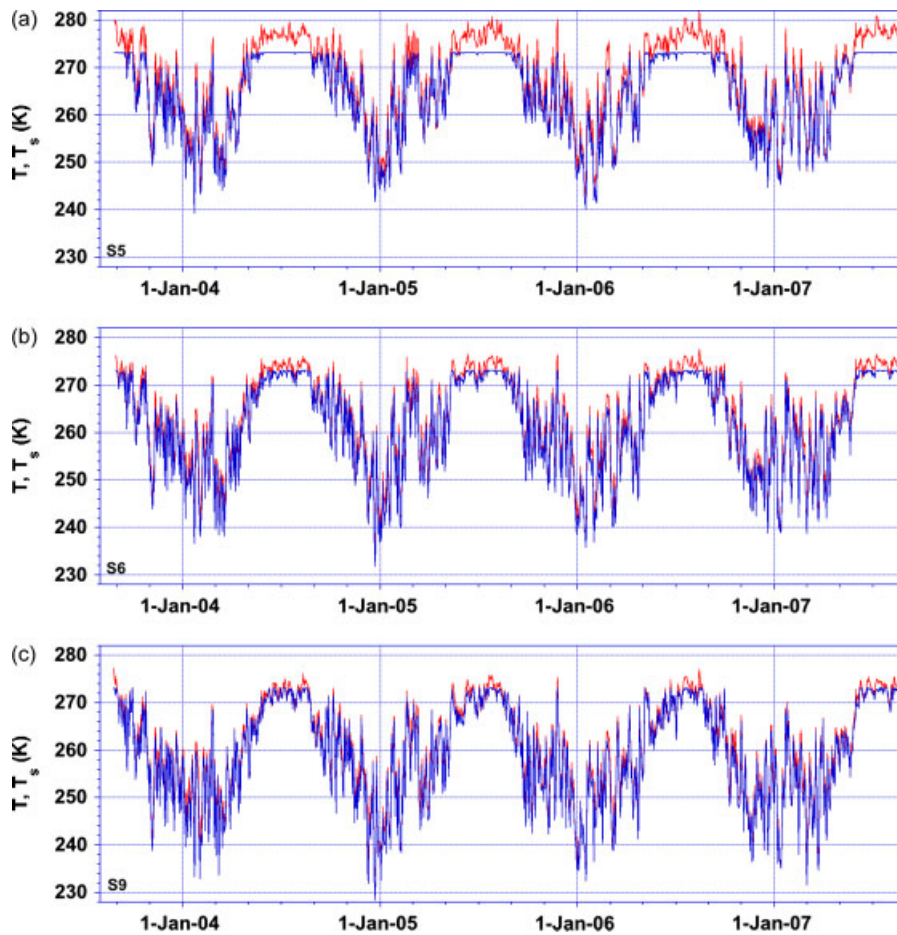


Figure 6. Daily mean surface temperature  $T_s$  (blue line) and 2 m temperature  $T_{2m}$  (red line) at (a) S5, (b) S6 and (c) S9. This figure is available in colour online at [www.interscience.wiley.com/ijoc](http://www.interscience.wiley.com/ijoc)

in which  $\rho$  is air density,  $c_p$  the heat capacity of dry air at constant pressure,  $L_s$  the latent heat of sublimation,  $w'$ ,  $\theta'$  and  $q'$  are the turbulent fluctuations of vertical velocity, potential temperature and specific humidity and  $u_*$ ,  $\theta_*$  and  $q_*$  are the associated turbulent scales. The turbulent scales are calculated using the ‘bulk’ method, a robust method that relates turbulence scales to differences in wind speed  $V$ , potential temperature  $\theta$  and specific humidity  $q$  between a single AWS or model measurement level and the snow surface:

$$u_* \cong \frac{\kappa[V(z_V) - V(z_{0,V})]}{\ln \frac{z_V}{z_{0,V}} - \Psi_m\left(\frac{z_V}{L_{MO}}\right)}; \theta_* \cong \frac{\kappa[\theta(z_T) - \theta(z_{0,T})]}{\ln \frac{z_T}{z_{0,T}} - \Psi_h\left(\frac{z_T}{L_{MO}}\right)}; \quad (2)$$

$$q_* \cong \frac{\kappa[q(z_q) - q(z_{0,q})]}{\ln \frac{z_q}{z_{0,T}} - \Psi_h\left(\frac{z_q}{L_{MO}}\right)}$$

where  $L_{MO}$  is the Monin-Obukhov length scale:

$$L_{MO} = \frac{u_*^2}{\kappa g / [\theta_* + 0.62 \theta q_*]} \quad (3)$$

and  $\kappa$  is the Von Kármán constant ( $\kappa = 0.4$ ),  $V$ ,  $\theta$  and  $q$  are wind speed, potential temperature and specific humidity measured at AWS sensor heights  $z_V$ ,  $z_T$  and

$z_q$ , respectively. The RH and T sensors are in the same housing so that  $z_q = z_T$ , while  $z_V$  is greater by about 0.75 m (Figure 2). Sensor heights ( $z_V$ ,  $z_q$  and  $z_T$ ) are tracked using data of the sonic height ranger.  $\psi_m$  and  $\psi_h$  are the vertically integrated stability correction functions for momentum and heat, respectively. For stable conditions ( $z/L_{MO} > 0$ ), we use the  $\psi_m = \psi_h$  function proposed by Holtslag and De Bruijn (1988), which behaves most consistently in the very stable limit where turbulence ceases (Andreas, 2002). For unstable conditions ( $z/L_{MO} < 0$ ), the functions of Dyer (1974) are used. By definition  $V(z_{0,V}) = 0$ . We assume the surface to be saturated, i.e.  $q(z_{0,q})$  is known when surface temperature  $T_s = T(z_{0,T})$  is known. This leaves the surface temperature  $T_s$  and the surface ‘roughness’ lengths for momentum, heat and moisture  $z_{0,V}$ ,  $z_{0,T}$  and  $z_{0,q}$  unknown (next sections).

### 3.2. Determination of surface temperature

Surface temperature  $T_s$  must be determined with sufficient accuracy, because sign and magnitude of SHF is determined by the difference between surface and air temperature. The surface temperature  $T_s$  is determined using:

$$\sigma T_s^4 = \frac{\epsilon - 1}{\epsilon} LW \downarrow - \frac{1}{\epsilon} LW \uparrow$$

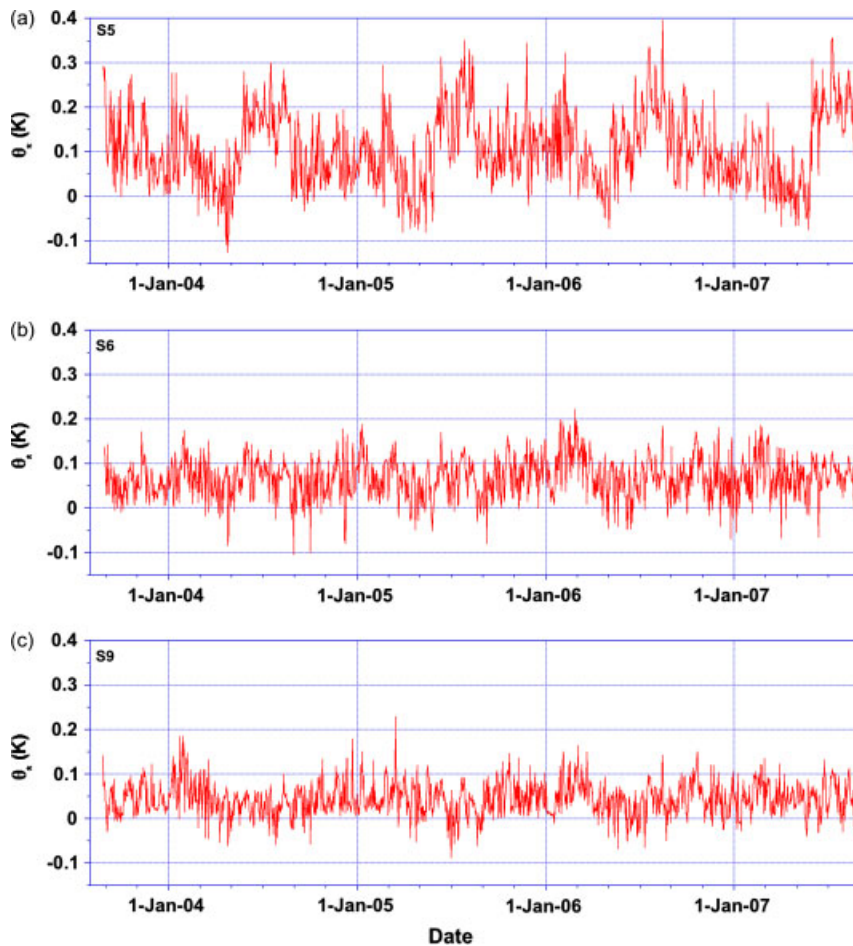


Figure 7. Daily mean turbulent temperature scale  $\theta_*$  at (a) S5, (b) S6 and (c) S9. This figure is available in colour online at [www.interscience.wiley.com/ijoc](http://www.interscience.wiley.com/ijoc)

$$= -LW \uparrow + \frac{\varepsilon - 1}{\varepsilon} LW_{net} \quad (4)$$

where  $\sigma = 5.67 \times 10^{-8} \text{ W m}^{-2} \text{ K}^{-4}$  is the Stefan-Boltzmann constant,  $\varepsilon$  the surface longwave emissivity (unknown) and  $LW_{net} = LW \uparrow + LW \downarrow$ . The radiation sensors used on the AWS are of secondary standard (Table I) and are furthermore unventilated and unheated. Van den Broeke *et al.* (2004) showed that hourly mean LW measurements typically have a root-mean-squared-error (RMSE) smaller than  $3 \text{ W m}^{-2}$ , corresponding to  $<0.7^\circ\text{C}$  uncertainty in  $T_s$ .

In this study we assume  $\varepsilon = 1$ , but Wiscombe and Warren (1980) state that  $\varepsilon$  may be as low as 0.98. The impact of this uncertainty on calculated  $T_s$  depends on  $LW_{net}$  through Equation (4). Extreme values of  $LW_{net}$  found in Greenland are  $0 \text{ W m}^{-2}$  under overcast conditions and  $-80 \text{ W m}^{-2}$  under clear sky, summertime conditions around noon (Van den Broeke *et al.*, 2008a). A positive bias of 0.02 in  $\varepsilon$  thus introduces a maximum underestimation of  $T_s$  of about 0.5 K for typical temperatures. This is an extreme value, more typical values will be 0.1–0.3 K. Because the value of  $\varepsilon$  is not known, we choose to accept this additional uncertainty in  $T_s$  and use  $\varepsilon = 1$ . Evidently, if  $T_s > 0^\circ\text{C}$ , it is reset to  $0^\circ\text{C}$ .

### 3.3. Calculation of $z_{0,v}$ , $z_{0,T}$ and $z_{0,q}$

$z_{0,v}$ ,  $z_{0,T}$  and  $z_{0,q}$  are the surface scalar ‘roughness’ lengths for momentum, heat and moisture, and represent the levels at which the wind, temperature and specific humidity values extrapolate towards their surface values. If  $z_{0,v}$  is known,  $z_{0,T}$  and  $z_{0,q}$  are calculated using the expressions of Andreas (1987) and the modified parameterisation for rough ice surfaces ( $z_{0,v} > 1 \text{ mm}$ ,  $Re^* > 2.5$ ) proposed by Smeets and Van den Broeke (2008b).

In the GrIS ablation zone, there is a strong spatial and temporal variation in  $z_{0,v}$  (Van den Broeke, 1996; Smeets and Van den Broeke, 2008a, henceforth SB08). We use the two-level measurements to calculate a running mean of  $z_{0,v}$ : all profiles in a 20-day window around the time of observation are collected ( $N = 480$ ), after which near-neutral wind profiles ( $|z/L_{MO}| < 0.1$ ) are selected for averaging, inversely weighing them with the time difference to the moment of observation. Owing to obstruction by the mast, insufficient reliable wind profiles were available at S9 in the first two years; for this site and period we prescribed the published values from SB08.

Figure 3 shows the resulting  $z_{0,v}$  time series, together with the 25-day-binned means of SB08. The latter are reproduced quite well. In spite of the rather long aver-

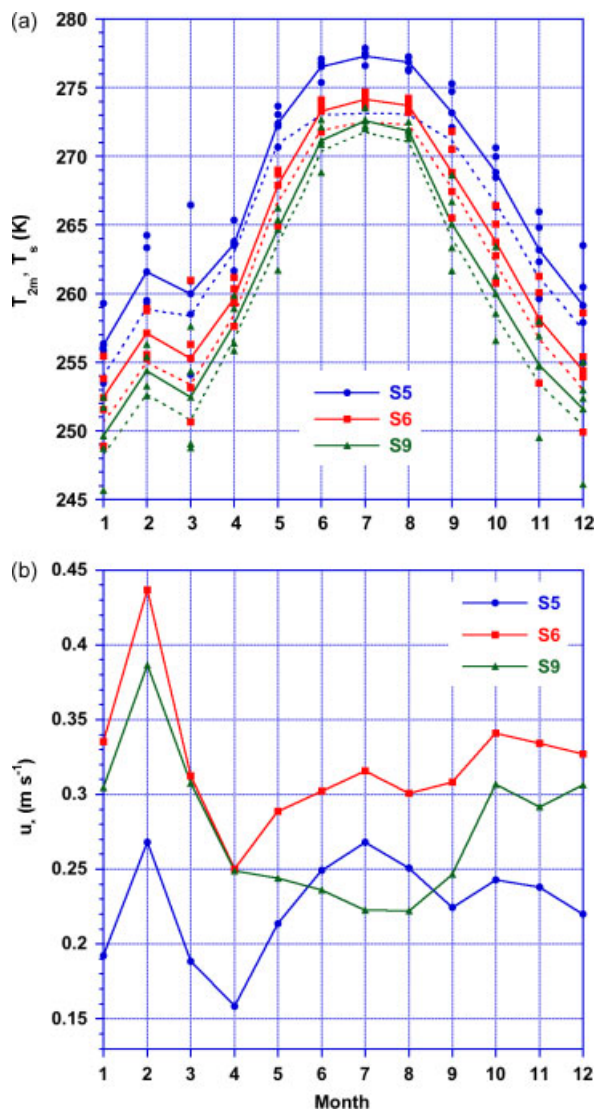


Figure 8. Average seasonal cycle, based on monthly means, of (a) surface temperature  $T_s$  and 2 m temperature  $T_{2m}$  (individual months indicated by symbols) and (b) turbulent temperature scale  $\theta_*$ . This figure is available in colour online at [www.interscience.wiley.com/ijoc](http://www.interscience.wiley.com/ijoc)

aging period of 20-days,  $z_{0,v}$  varies quickly in time, in line with earlier findings. SB08 showed that not the large ice hills, but rather the smaller roughness elements (the 'ice cubes' at the surface and the gullies and smaller hummocks) determine the value of  $z_{0,v}$ . This is confirmed by Figure 3, which shows that the largest values of  $z_{0,v}$  occur at S6 ( $z_{0,v} \sim 2.5$  cm), rather than at S5 ( $z_{0,v} \sim 1$  cm) in spite of the larger ice hills. At S9, the highest  $z_{0,v}$  values occurred after the anomalously strong melt summer of 2007, when glacier/superimposed ice briefly reached the surface (Van den Broeke *et al.*, 2008b). Note that the wintertime minimum at S6 was reduced in 2005–2006 and 2006–2007, probably associated with less winter snowfall.

At S5 and S6, a clear seasonal cycle emerges from the monthly means of  $z_{0,v}$  (Figure 4). Especially at S5, a distinct minimum is reached in spring before the onset of the melting season, followed by a gradual increase and a

summertime maximum in July/August. No clear seasonal cycle emerges at S9, a result of the large variability in summer when (superimposed) ice may or may not reach the surface.

#### 3.4. Validation of calculated turbulent fluxes

Figure 5 compares hourly mean SHF and LHF as calculated using the bulk method with direct eddy correlation measurements. First, measured 10-min average fluxes were selected based on strict criteria (Smeets and Van den Broeke, 2008b). After that, it was imposed that all six 10-min mean values were available to calculate hourly means to compare with the hourly bulk fluxes from the AWS. This procedure left 417 hourly values of SHF and 223 of LHF. With regression coefficients of 0.68 and 0.74, agreement is reasonable, but with regression slopes less than unity and a significant bias, agreement is less good than for a similar comparison of Antarctic data (Van den Broeke *et al.*, 2005). This can likely be attributed to the much greater seasonal variability in the nature of the GrIS surface, which introduces, e.g., an unknown displacement distance. New eddy correlation data that are presently being collected at S5 will hopefully reduce the uncertainty.

## 4. Results

Table II lists the main topographical and annual climate/mass balance characteristics of the AWS sites during the period August 2003–August 2007. S5 and S6 experience a net annual ablation of  $-3.8$  and  $-1.4$  m, water equivalent (w.e.), respectively, while S9 is close to the equilibrium line. The main goal of this section is to interpret the turbulent scales of momentum ( $u_*$ ), heat ( $\theta_*$ ) and moisture ( $q_*$ ) in terms of climatic surface-to-air gradients in SL wind speed ( $V_{10m}$ ), temperature ( $T_{2m}$ ) and humidity ( $q_{2m}$ ). Next, the turbulent fluxes of sensible heat ( $\sim u_* \theta_*$ ) and latent heat ( $\sim u_* q_*$ ) can be conveniently interpreted in terms of the products of the turbulent scales.

#### 4.1. Temperature and turbulent temperature scale $\theta_*$

Table II shows that the lapse rate of annual mean  $T_{2m}$  is sub-adiabatic, as the surface is melting for part of the year, which damps the seasonal amplitude. Figures 6 and 7 show daily mean  $T_{2m}$  and  $T_s$  and the turbulent temperature scale  $\theta_*$ , respectively, while Figure 8 shows the average seasonal cycle of these variables, based on monthly means. Daily mean  $T_{2m}$  is higher than  $T_s$  (i.e. the SL is stably stratified and  $\theta_* > 0$ ) for 92% (S5), 94% (S6) and 90% (S9) of the days. In wintertime, the surface temperature deficit is maintained by a negative surface radiation budget (Van den Broeke *et al.*, 2008a). In summer, the melting surface is responsible for the stable stratification. Only at S5 is summer melting continuous over the day, resulting in prolonged periods during which daily mean  $T_s = 0^\circ\text{C}$  (Figure 6(a)). At S6 and S9, the surface frequently refreezes during the night, resulting

Table II. AWS topographic, climate and turbulence characteristics.

	S5	S6	S9
<i>Location (August 2006)</i>			
Latitude (N)	67°06'	67°05'	67°03'
Longitude (W)	50°07'	49°23'	48°14'
Elevation (m asl)	490	1020	1520
Distance from ice edge (km)	6	38	88
<i>Period of operation used for this paper</i>			
Start of observation	28 Aug 2003	1 Sep 2003	1 Sep 2003
End of observation	27 Aug 2007	31 Aug 2007	31 Aug 2007
<i>Annual mean climate variables</i>			
Mass balance (m w.e.)	-3.6	-1.5	~0
Pressure (hPa)	950	887	835
2 m temperature (K)	267.4	263.2	260.5
Density (kg m <sup>-3</sup> )	1.24	1.17	1.12
Surface temperature (K)	265.1	261.7	259.3
2 m relative humidity (%)	75	87	90
2 m specific humidity (g kg <sup>-1</sup> )	2.4	2.2	1.9
10 m wind speed (m s <sup>-1</sup> )	5.3	6.9	7.8
Wind directional constancy	0.86	0.89	0.82
<i>Annual mean turbulence variables</i>			
SHF (W m <sup>-2</sup> )	36	28	15
LHF (W m <sup>-2</sup> )	-6	-2	-2
log( $z_{0,v}$ ) (m)	-2.9	-2.7	-3.9
log( $z_{0,T}$ ) (m)	-3.1	-3.2	-4.1
$u_*$ (m s <sup>-1</sup> )	0.23	0.32	0.28
$\theta_*$ (K)	0.11	0.07	0.04
$q_*$ (10 <sup>-3</sup> g kg <sup>-1</sup> )	-6.6	-2.0	-2.8

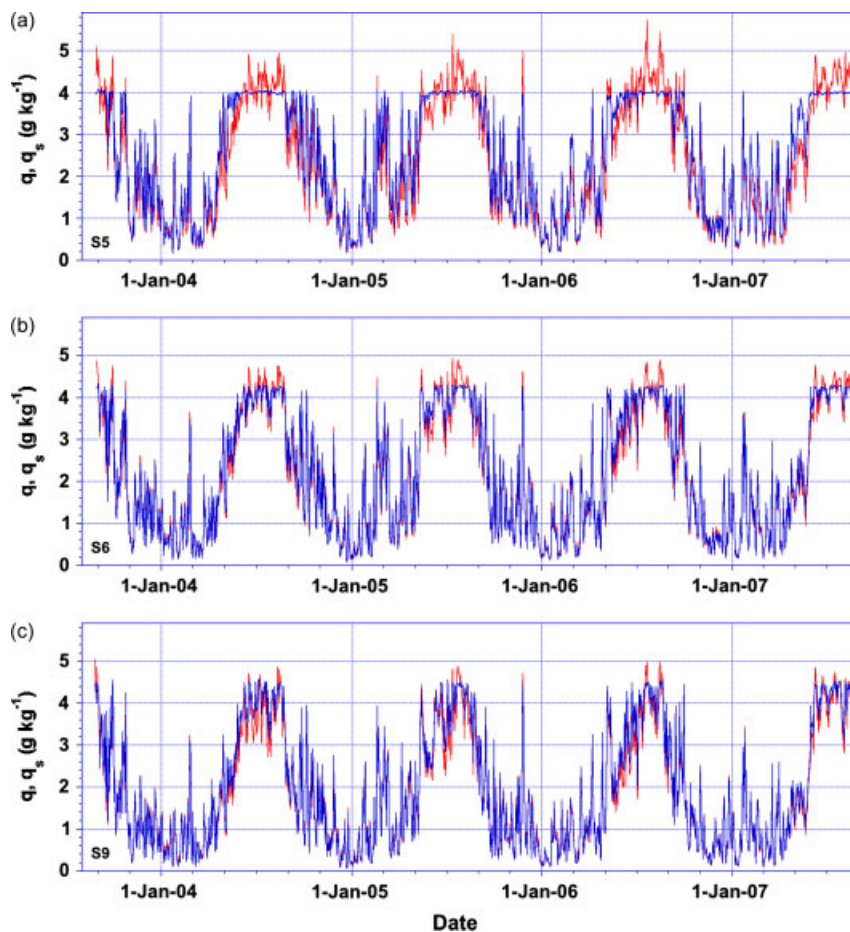


Figure 9. Daily mean surface specific humidity  $q_s$  (blue line) and 2 m specific humidity  $q_{2m}$  (red line) at (a) S5, (b) S6 and (c) S9. This figure is available in colour online at [www.interscience.wiley.com/ijoc](http://www.interscience.wiley.com/ijoc)

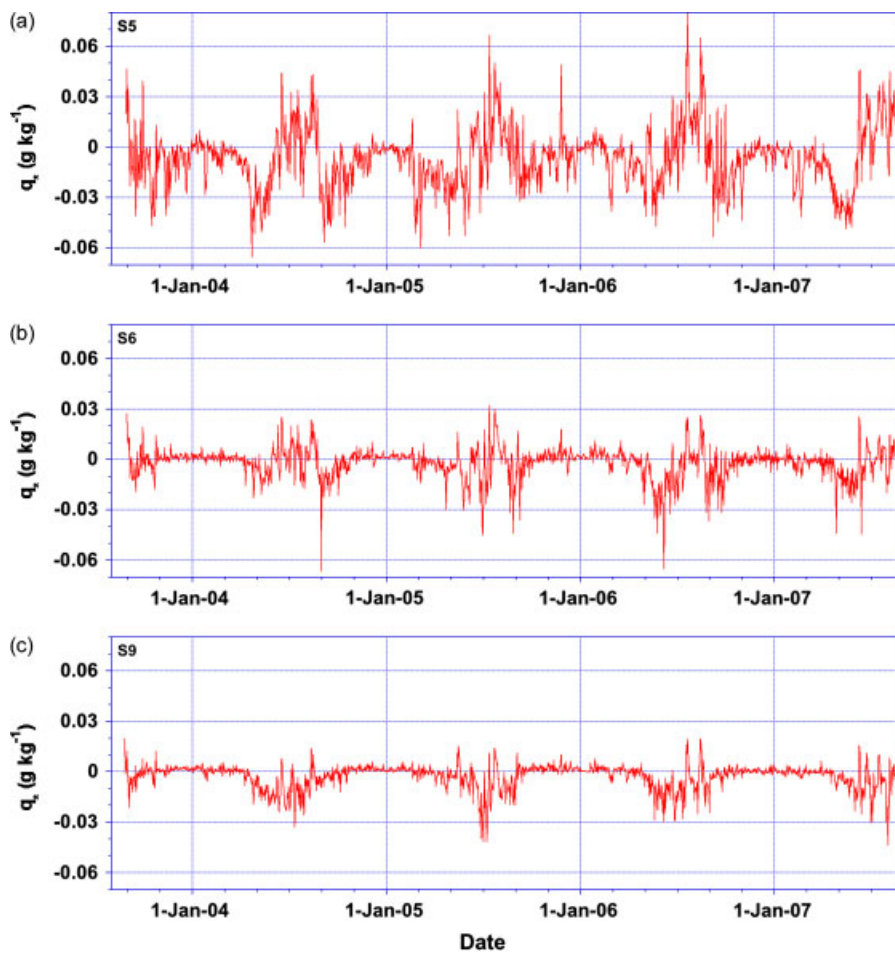


Figure 10. Daily mean turbulent humidity scale  $q_*$  at (a) S5, (b) S6 and (c) S9. This figure is available in colour online at [www.interscience.wiley.com/ijoc](http://www.interscience.wiley.com/ijoc)

in daily mean  $T_s < 0^\circ\text{C}$  (Figure 6(b), (c)). In winter, when warm air masses are advected towards the ice sheet, temperature may increase by 20–30 K in a single day. As a result, interannual variability in monthly mean temperature is largest in winter (Figure 8(a)).

At S6 and S9, the largest values of  $\theta_*$  are found in late winter (Figures 7 and 8(b)), forced by radiative cooling of the surface. At S5, in contrast, the largest absolute surface-to-air temperature gradients are found in summer, with daily mean values in excess of  $4^\circ\text{C m}^{-1}$  (Figure 6(a)). But strong inversions alone are not sufficient to generate large values of  $\theta_*$ : in order for the stability correction to remain small ( $\Psi_h$  in Equation (2)),  $L_{MO}$  and thus wind shear  $u_*$  must be sufficiently large; katabatic forcing ensures that this is the case (see Section 4.3 and Van den Broeke *et al.*, 2005). The large temperature gradient in combination with strong mixing sustains large positive values of  $\theta_*$  at S5 during summer with typical values of 0.15–0.25 K (Figure 7(a)). Wintertime  $\theta_*$  values at S5 show larger interdiurnal variability, because surface temperature can freely adjust to changes in the surface energy budget. For example, when the sky becomes overcast in winter, the longwave radiation deficit at the surface vanishes, generating a near-neutral SL with  $\theta_* \sim 0$  K. In summer, the temperature gradient

persists due to the melting ice surface; the additional energy available at the surface is then invested in melting.

A notable feature is the frequent occurrence of convection (negative  $\theta_*$ ) at S5 in spring (March, April, May, Figure 7(a)). The reason is that a relatively dark ice surface with albedo  $\sim 0.6$ – $0.7$  is present at S5 already before the onset of melt (Van den Broeke *et al.*, 2008a). This enhances the absorption of solar radiation at the surface to which  $T_s$  can freely adjust and hence rise above  $T_{2m}$ .

The seasonal cycle of  $\theta_*$  (Figure 8(b)) shows quite different behaviour at the three sites. At S9,  $\theta_*$  peaks in late winter when surface cooling by longwave radiation is strongest and the surface-to-air temperature gradient is largest. At S6, we see a similar winter peak in  $\theta_*$ , but a secondary summer peak resulting from the melting surface. At S5, the summer peak in  $\theta_*$  becomes dominant over the winter peak, while the pronounced April minimum in  $\theta_*$  reflects the frequent occurrence of convection, as discussed above.

#### 4.2. Humidity and turbulent moisture scale $q_*$

Annual mean 2 m relative humidity ( $\text{RH}_{2m}$ ) decreases towards the ice margin (Table II), but specific humidity ( $q_{2m}$ ) increases, in response to higher air temperatures. Figures 9 and 10 show daily average values of  $q_{2m}$ ,  $q_s$

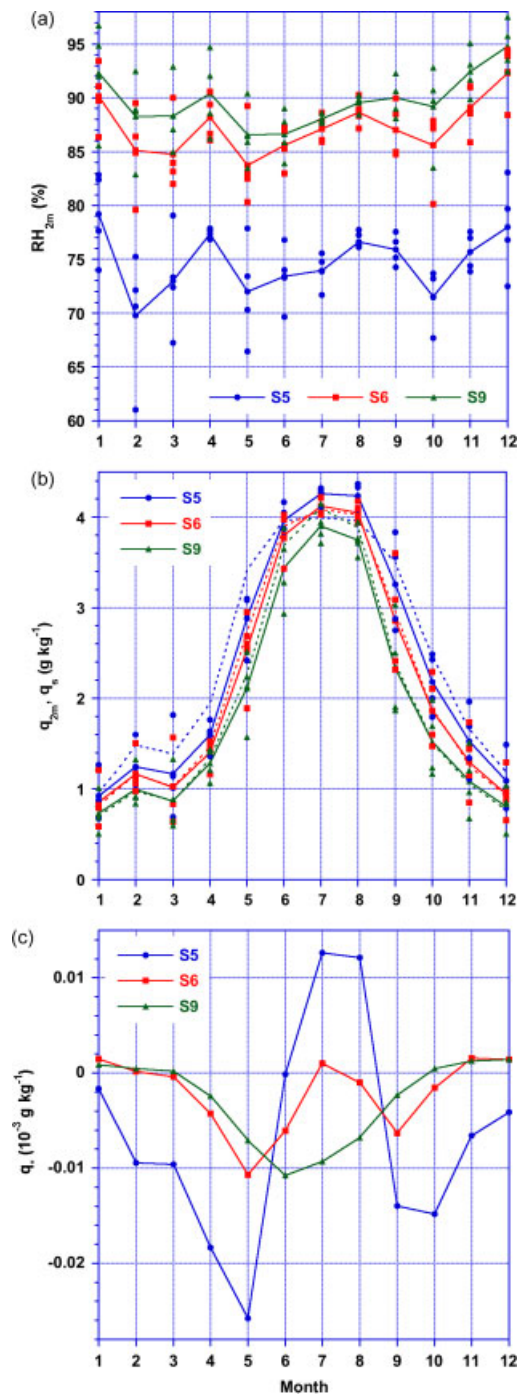


Figure 11. Average seasonal cycle, based on monthly means, of (a) 2 m relative humidity (individual months indicated by symbols), (b) surface and 2 m specific humidity  $q_s$  and  $q_{2m}$  (individual months indicated by symbols) and (c) turbulent humidity scale  $q_*$ . This figure is available in colour online at [www.interscience.wiley.com/ijoc](http://www.interscience.wiley.com/ijoc)

and  $q_*$ ; Figure 11 shows the average seasonal cycle of these variables and that of 2 m relative humidity ( $RH_{2m}$ ). With differences of less than 10% between the extreme months,  $RH_{2m}$  does not show a clear seasonal cycle at any of the sites (Figure 11(a)). As a result,  $q_{2m}$  (Figure 9) mainly follows  $T_{2m}$  with enhanced sensitivity at higher temperatures according to Clausius–Clapeyron's relation.

In contrast to temperature, the surface-to-air specific humidity gradient does not maintain the same sign

throughout the year. In response to low temperatures, the wintertime values of  $q$  and that of its vertical gradients and thus  $q_*$  are small at all sites.  $RH_{2m}$  and  $T_{2m}$  at S9 and S6 are sufficiently high to cause small positive values of  $q_*$  signifying deposition (Figure 10(b), (c)). At S5, where RH is relatively low (Figure 11(a)), the wintertime gradient in  $q$  remains directed from surface to air (negative  $q_*$ ), signifying sublimation (Figure 10(a)).

In spring at S5, the low surface albedo in combination with the non-melting surface causes sublimation, i.e. strongly negative values of  $q_*$ , typically  $-0.03$  to  $-0.05 \text{ g kg}^{-1}$  (Figure 10(a)). In spring and summer, the snow surface at S9 is heated leading to sublimation (negative  $q_*$ ) from May onwards (Figure 10(c)). At these higher temperatures, the magnitude of  $q_*$  is much larger than in winter. Regular intrusions of warm, humid air during summer can cause surface melting at S9, temporarily reversing the gradient and making  $q_*$  positive (deposition, Figure 10(c)). At S6, these reversals are more pronounced, in response to higher temperatures and a frequently melting surface. At S5, near-continuous surface melting during summer causes a semi-permanent positive  $q_*$  but with large interdiurnal variations (Figure 10(a)).

At S9, the seasonal cycle of  $q_*$  (Figure 11(c)) is symmetrical curve the summer solstice, reflecting the dominant influence of summertime heating in the absence of continuous melting. At S6, frequent surface melting from June onwards causes the downward trend in monthly mean  $q_*$  to reverse in June, with values becoming slightly positive in July. At S5, monthly mean  $q_*$  becomes negative (sublimation) in March and April similar to  $\theta_*$  as discussed above. When melting starts, the gradient reverses, leading to positive monthly mean  $q_*$  values in July and August, indicative of condensation.

#### 4.3. Wind speed and friction velocity $u_*$

Table II lists annual mean values of 10 m wind speed ( $V_{10m}$ ); Figure 12 shows daily mean  $V_{10m}$ , and Figure 13 shows the seasonal cycle of wind directional constancy  $V_{10m}$  and friction velocity  $u_*$  based on monthly means. There are several indications that katabatic forcing is the dominant driving force of SL winds in the Greenland ablation zone: (1) the high wind directional constancy (DC), ranging from 0.82 to 0.89 (Table II, Figure 13(a)); (2) the fact that daily mean wind speed never quite becomes zero (Figure 12) and (3) the mean south-easterly wind direction (Van den Broeke *et al.*, 1994; Denby *et al.*, 2002), signifying downslope forcing turned to the right by the Coriolis effect.

Katabatic winds are ultimately driven by cooling of the SL air through a downward directed SHF (positive  $\theta_*$ ), which in the winter can only be sustained by radiational cooling of the surface. Figure 14 demonstrates the close linkage between monthly mean wind speed and the surface radiation budget. When the radiation balance is negative (late autumn, winter, early spring), SL wind speed and radiative cooling are closely coupled, the highest wind speeds occurring when the radiational cooling is

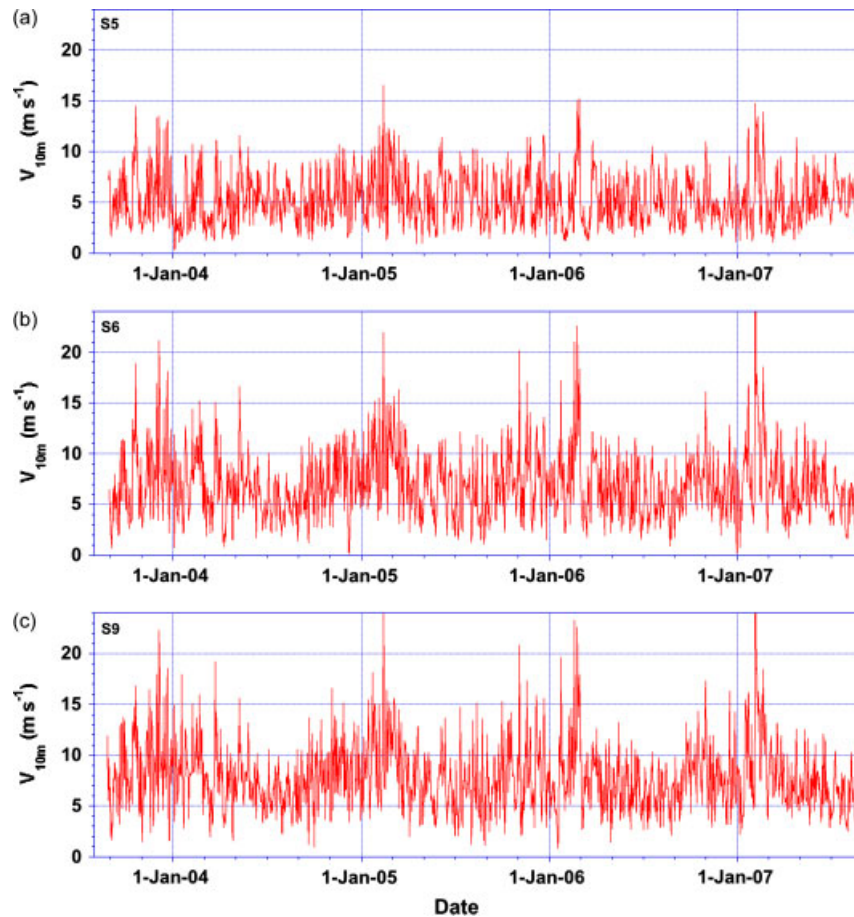


Figure 12. Daily mean 10 m wind speed  $V_{10m}$  at (a) S5, (b) S6 and (c) S9. This figure is available in colour online at [www.interscience.wiley.com/ijoc](http://www.interscience.wiley.com/ijoc)

largest. When the surface radiation balance becomes positive (late spring, summer and early autumn) this coupling largely disappears. An exception is S5, where katabatic forcing persists in summer. These summertime katabatic winds are often called glacier winds, for they are frequently observed over melting valley glaciers in summer.

The product of temperature deficit and surface slope determines katabatic forcing, so one would expect the average wind speed to increase towards the ice sheet margin. The opposite trend in  $V_{10m}$  that is observed towards the ice margin is caused by (1) the greater surface roughness in the crevassed terrain at the margin during summer, limiting near surface wind speeds and (2) the piling up of cold air over the flat tundra in winter, which sets up a reverse pressure gradient force and slows down the winds in the marginal zone (Van den Broeke *et al.*, 1994). This phenomenon has also been observed over the Antarctic ice sheet and adjacent ice shelves (Gallée and Schayes, 1992; Van den Broeke *et al.*, 2002; Renfrew, 2004). In summer, when convection over the snow-free tundra has removed the cold air layer, wind speed differences between the sites become smaller (Figure 13(b)). But during the night, the mechanism is still active, causing a pronounced daily cycle in wind speed near the ice margin (not shown here, see Van den Broeke *et al.*, 1994).

The seasonal cycle of DC (Figure 13(a)) also supports the katabatic nature of the SL winds. At S9, the maximum DC is reached in winter, when the radiation deficit is largest, with lower values in summer. At S5 and S6, a second peak is observed in summer, when the glacier wind mechanism becomes active. A minimum in DC occurs in March/April at all three sites, the months with frequent convection (see previous section). Convection enhances momentum exchange with the free atmosphere, reducing the directional constancy of the SL winds.

The seasonal cycle of  $V_{10m}$  (Figure 13(b)) shows that February, consistently, is the month with the highest wind speed. This is also the month with the largest radiation deficit, caused by low cloud cover (Van den Broeke *et al.*, 2008a), arguably a result of sea ice reaching its southernmost extent in this month, reducing the role of the ocean as moisture source for cloud formation. At S9,  $V_{10m}$  monotonously decreases to reach a minimum in August, in line with the smaller radiation deficit. At S5, a secondary summer maximum in  $V_{10m}$  is observed as a result of the glacier wind mechanism described above.

The seasonal cycle in friction velocity  $u_*$  (Figure 13(c)) qualitatively follows  $V_{10m}$  but is modified by the seasonal variations in  $z_{0,V}$ , which enhances the summertime  $u_*$  at S5 and S6. These high summertime  $u_*$  values are necessary to sustain the mechanical generation

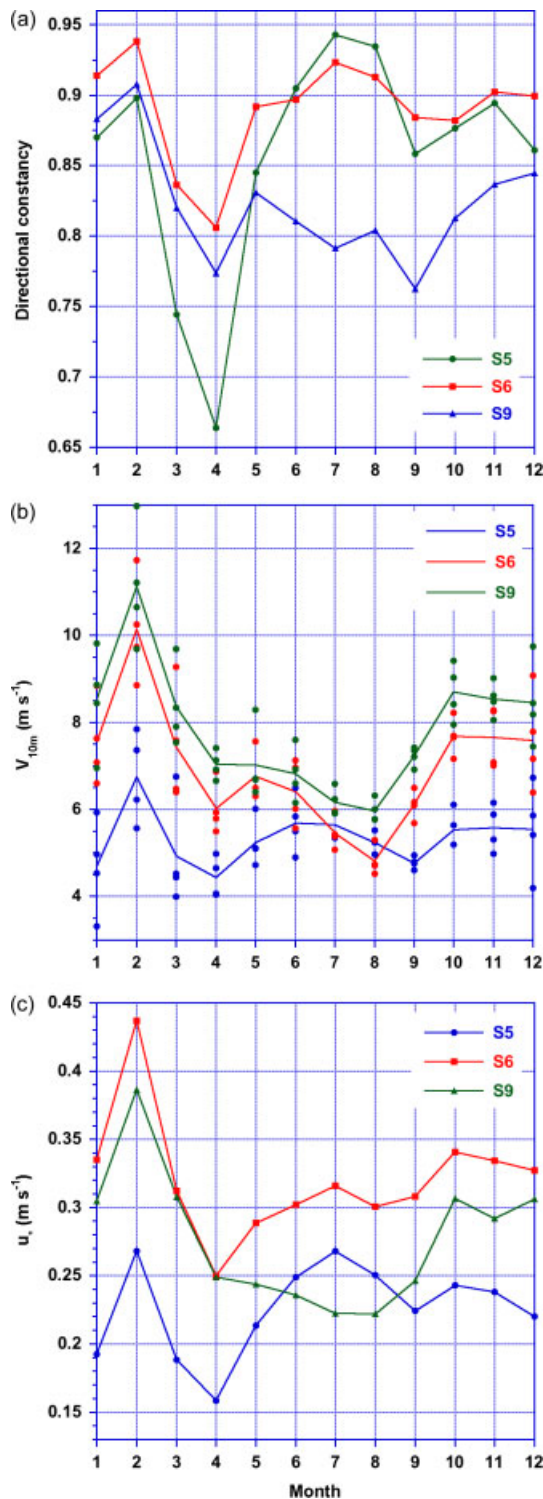


Figure 13. Average seasonal cycle, based on monthly means, of (a) wind directional constancy, (b) 10 m wind speed  $V_{10m}$  (individual months indicated by symbols) and (c) turbulent velocity scale  $u_*$ . This figure is available in colour online at [www.interscience.wiley.com/joc](http://www.interscience.wiley.com/joc)

of turbulence in the strongly stratified SL over the melting ice surface in the lower ablation zone (see next section).

#### 4.4. Turbulent fluxes of sensible and latent heat

Analysis of the temporal variability of the turbulent fluxes of SHF and LHF can now be conveniently based

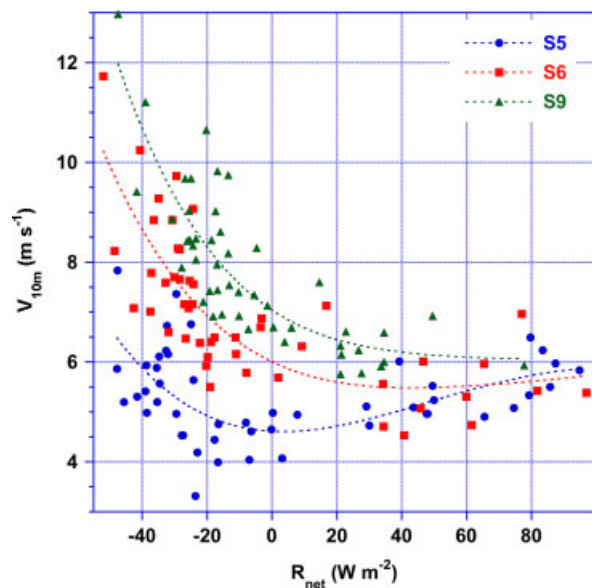


Figure 14. Monthly mean wind speed ( $N = 48$ ) as a function of net surface radiation. This figure is available in colour online at [www.interscience.wiley.com/joc](http://www.interscience.wiley.com/joc)

on the previous sections, because they vary with the products of the turbulent scales: SHF  $\sim u_* \theta_*$  and LHF  $\sim u_* q_*$ . Table II shows annual means of SHF and LHF; Figures 15 and 16 the daily averages and Figure 17 the seasonal cycles based on monthly means.

Daily mean SHF (Figure 15) is generally positive but shows large interdiurnal variability and at S5 attains maximum values in excess of  $200 W m^{-2}$ , which is considerable given the strong stratification of the SL. Weak convection (SHF  $< 0$ ) occurs regularly in early spring at S5, late spring at S6 and in summer at S9, which coincides with the period that the surface is heated by the absorption of solar radiation but has not yet reached the melting point.

The magnitude of daily mean LHF (Figure 16) is generally much smaller than SHF. At S5, where  $RH_{2m}$  is lowest, sublimation dominates and changes to deposition/condensation only in summer. At S6, weak deposition in winter changes to sublimation in spring, and occasional deposition/condensation in summer. At S9, these summer reversals from sublimation to deposition occur least frequently, and sublimation dominates in summer.

Annual mean SHF increases strongly towards the ice margin, by nearly a factor of two between S9 and S6 and by 30% between S6 and S5 (Table II). According to the seasonal cycle (Figure 17(a)), the difference can be fully ascribed to the summer months JJA, when SHF at S5 is six to seven times greater than at S9 and two to three times greater than at S6. This difference in turn can be ascribed mostly to  $\theta_*$  (Figure 8(b)). These large summertime values of SHF are made possible by the positive coupling of  $u_*$  and  $\theta_*$  through the katabatic forcing and the rough ice surface, keeping  $u_*$  large even under strong static stability.

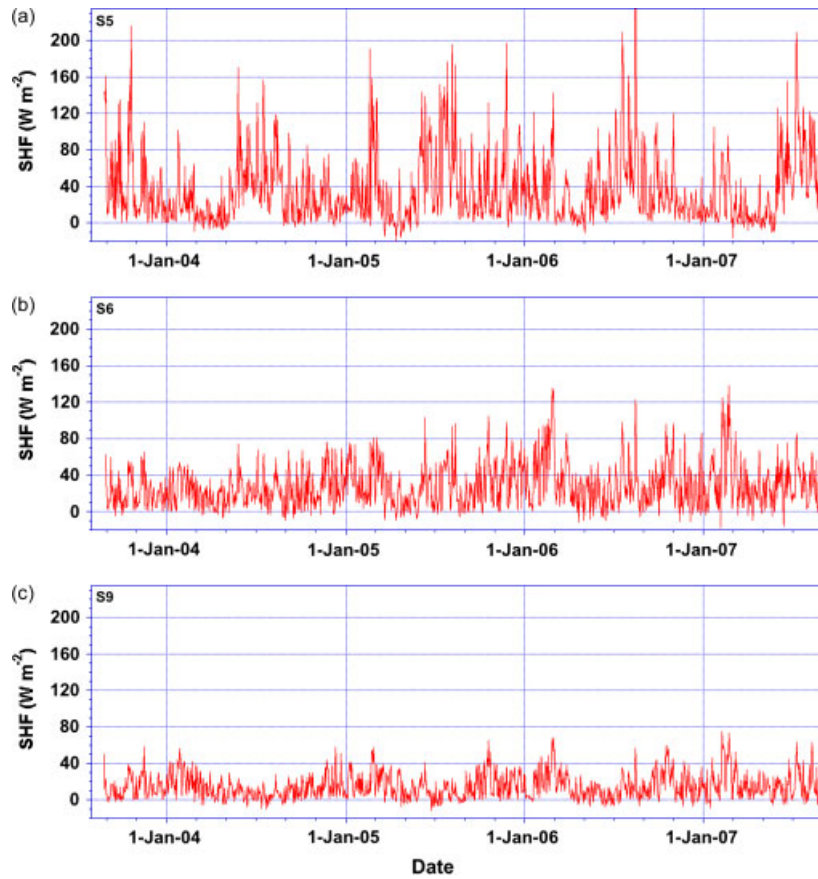


Figure 15. Daily mean sensible heat flux (SHF) at (a) S5, (b) S6 and (c) S9. This figure is available in colour online at [www.interscience.wiley.com/ijoc](http://www.interscience.wiley.com/ijoc)

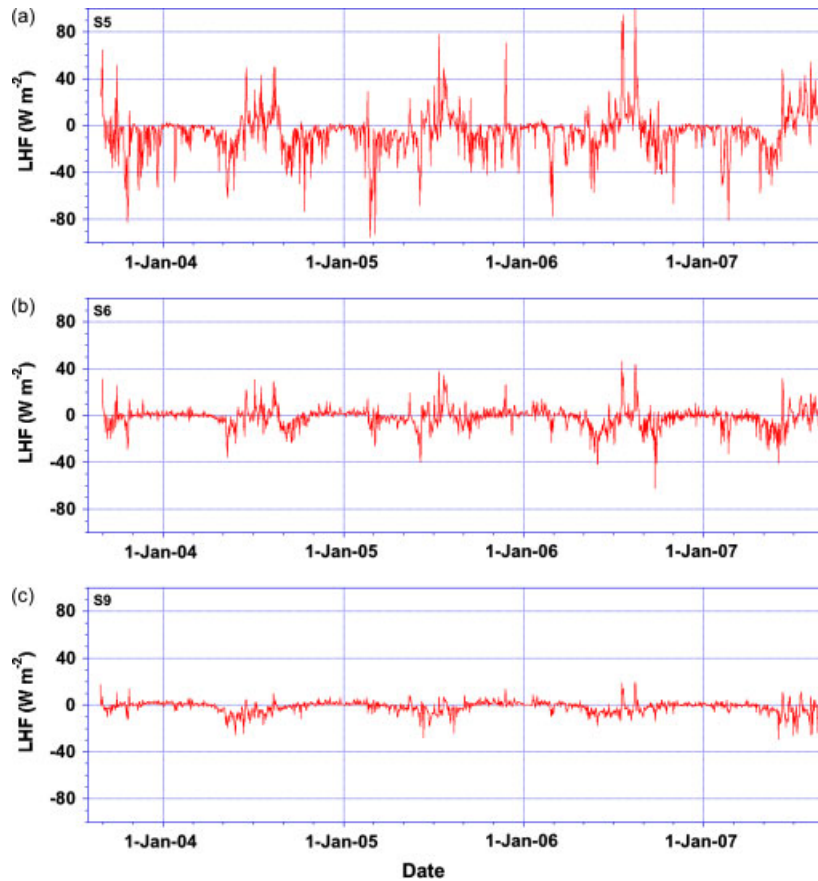


Figure 16. Daily mean latent heat flux (LHF) at (a) S5, (b) S6 and (c) S9. This figure is available in colour online at [www.interscience.wiley.com/ijoc](http://www.interscience.wiley.com/ijoc)

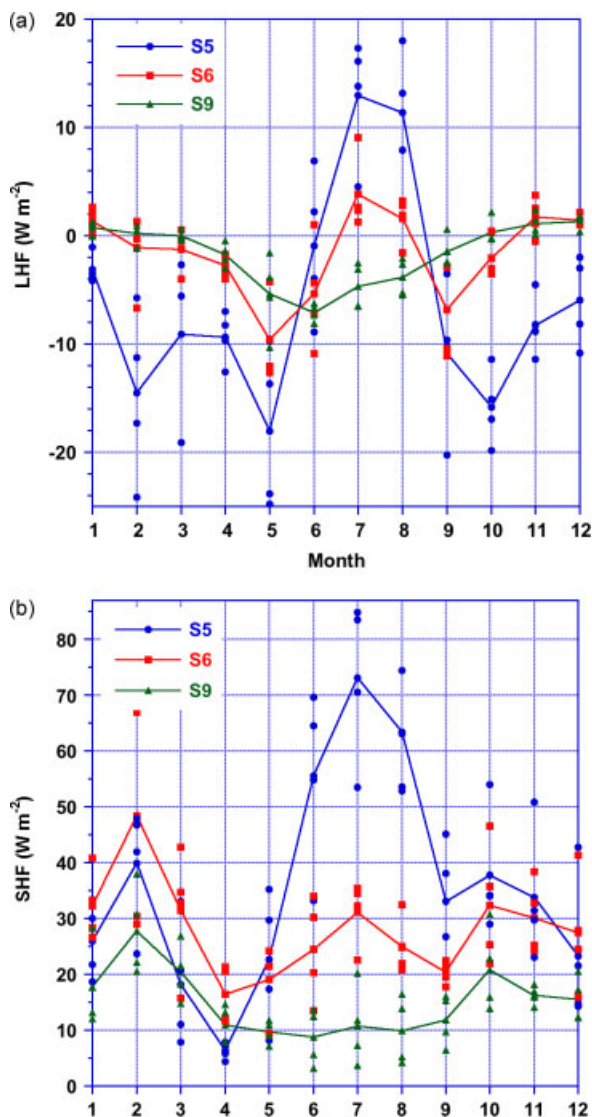


Figure 17. Average seasonal cycle, based on monthly means, of (a) sensible heat flux (SHF) and (b) latent heat flux (LHF). This figure is available in colour online at [www.interscience.wiley.com/ijoc](http://www.interscience.wiley.com/ijoc)

At S9, weak winter deposition (Figure 17(b)) is followed by moderate sublimation in summer. At S9, the magnitude of the summertime surface heat loss through LHF is approximately equal to the heat gain by SHF, in agreement with experiments performed close to the equilibrium line (Greuell and Konzelmann, 1994; Henneken *et al.*, 1994). At S6, summer melting causes sublimation to change into weak condensation in July and August, enhancing melt. At S5, LHF is a significant heat gain in summer and a significant heat sink in the remainder of the year. At S5 and S6, the sum of SHF and LHF in summer represents a considerable transport of heat to the surface, making a positive contribution to ice melt.

## 5. Summary and conclusions

Four years of AWS data collected at three sites in the west Greenland ablation zone have been used to describe the SL climate and turbulent fluxes of SHF and LHF. The SL

is stably stratified for 90–94% of the days, resulting in a downward directed SHF. In winter, radiational cooling of the surface maintains the stable stratification, while in summer, the melting ice surface remains colder than the overlying air. In spring, convection regularly occurs close to the ice margin as a result of the rapidly warming dark ice surface that has not yet reached the melting point. As a result of the near-continuous stable stratification, the SL wind climate in the Greenland ablation zone has a clear katabatic signature with high directional constancy. In combination with the rough ice surface, the glacier wind maintains the wind shear necessary to generate continuous turbulence in the stably stratified SL, resulting in July mean SHF as large as  $70 \text{ W m}^{-2}$  in the marginal ice zone. The melting ice surface changes LHF from a surface heat sink into a heat source ( $\sim 5\text{--}15 \text{ W m}^{-2}$ ). In the higher ablation zone, the LHF is slightly positive in winter (deposition) and becomes negative in summer (sublimation), where it cancels the SHF.

## Acknowledgements

We thank IMAU technicians Wim Boot, Henk Snellen and Marcel Portanger for technical and computer support. This work is funded by Utrecht University and the Netherlands Arctic Program (NAP) of the Netherlands Organisation of Scientific Research, section Earth and Life Sciences (NWO/ALW).

## References

- Anderson PS. 1994. A method for rescaling humidity sensors at temperatures well below freezing. *Journal of Atmospheric and Oceanic Technology* **11**: 1388–1391.
- Andreas EL. 1987. A theory for the scalar roughness and the scalar transfer coefficients over snow and sea ice. *Boundary-Layer Meteorology* **38**: 159–184.
- Andreas EL. 2002. Parameterizing scalar transfer over snow and ice: a review. *Journal of Hydrometeorology* **3**: 417–432.
- Bamber JL, Ekholm S, Krabill WB. 2001. A new, high-resolution digital elevation model of Greenland fully validated with airborne altimeter data. *Journal of Geophysical Research* **106**: 6,733–6,745.
- Bøggild CE, Reeh N, Oerter H. 1994. Modelling ablation and mass-balance sensitivity to climate change of Storstrømmen, northeast Greenland. *Global and Planetary Change* **9**: 79–90.
- Box JE, Bromwich DH, Veenhuis BA, Bai L-S, Stroeve JC, Rogers JC, Steffen K, Haran T, Wang S-H. 2006. Greenland ice sheet surface mass balance variability (1988–2004) from calibrated Polar MM5 output. *Journal of Climate* **19**: 2783–2800.
- Braithwaite RJ. 1995. Positive degree-day factors for ablation on the Greenland ice sheet studied by energy balance modelling. *Journal of Glaciology* **41**: 153–160.
- Cassano JJ, Box JE, Bromwich DH, Li L, Steffen K. 2001. Evaluation of Polar MM5 simulations of Greenland's atmospheric circulation. *Journal of Geophysical Research* **106**: 33,867–33,890.
- Cazenave A. 2006. How fast are the ice sheets melting? *Science* **314**: 1250–1252.
- Denby B, Greuell JW, Oerlemans J. 2002. Simulating the Greenland atmospheric boundary layer. Part II: Energy balance and climate sensitivity. *Tellus* **54**: 529–541.
- Dethloff K, Schwager M, Christensen JH, Kiilsholm S, Rinke A, Dorn W, Jung-Rothenhäusler F, Fischer H, Kipfstuhl S, Miller H. 2002. Recent greenland accumulation estimated from regional climate model simulations and ice core analysis. *Journal of Climate* **15**: 2821–2832.
- Dyer AJ. 1974. A review of flux-profile relationships. *Boundary-Layer Meteorology* **7**: 363–372.

- Fettweis X. 2007. Reconstruction of the 1979–2006 Greenland ice sheet surface mass balance using the regional climate model MAR. *Cryosphere* **1**: 21–40.
- Gallée H, Schayes G. 1992. Dynamical aspects of katabatic winds evolution in the Antarctic coastal zone. *Boundary-Layer Meteorology* **59**: 141–161.
- Greuell WG, Konzelmann T. 1994. Numerical modelling of the energy balance and the englacial temperature of the Greenland Ice Sheet. Calculations for the ETH-Camp location (West Greenland, 1155 m a.s.l.). *Global and Planetary Change* **9**: 91–114.
- Henneken EAC, Bink NJ, Vugts HF, Cannemeijer F, Meesters AGCA. 1994. A case study of the daily energy balance near the equilibrium line on the Greenland ice sheet. *Global and Planetary Change* **9**: 69–78.
- Holtlag AAM, De Bruijn EIF. 1988. Applied modelling of the nighttime surface energy balance over land. *Journal of Applied Meteorology* **27**: 689–704.
- Lemke P, Ren J, Alley RB, Allison I, Carrasco J, Flato G, Fujii Y, Kaser G, Mote P, Thomas RH, Zhang T. 2007. Observations: changes in snow, ice and frozen ground. In *Climate Change 2007: The Physical Science Basis. Contribution of Working Group I to the Fourth Assessment Report of the Intergovernmental Panel on Climate Change*, Solomon S, Qin D, Manning M, Chen Z, Marquis M, Averyt KB, Tignor M, Miller HL (eds). Cambridge University Press: United Kingdom, New York.
- Oerlemans J, Grisogono B. 2002. Glacier wind and parameterization of the related surface heat flux. *Tellus* **54A**: 440–452.
- Renfrew IA. 2004. The dynamics of idealized katabatic flow over a moderate slope and ice shelf. *Quarterly Journal of the Royal Meteorological Society* **130**: 1023–1045.
- Smeets CJPP, Van den Broeke MR. 2008a. Parameterizing scalar roughness over smooth and rough ice surfaces. *Boundary-Layer Meteorology* **128**: 339–355.
- Smeets CJPP, Van den Broeke MR. 2008b. Temporal and spatial variation of momentum roughness length in the ablation zone of the Greenland ice sheet. *Boundary-Layer Meteorology* **128**: 315–338.
- Steffen K, Box JE. 2001. Surface climatology of the Greenland ice sheet: Greenland Climate Network 1995–1999. *Journal of Geophysical Research* **106**(D24): 33951–33964.
- Van den Broeke MR. 1996. Characteristics of the lower ablation zone of the west Greenland ice sheet for energy-balance modelling. *Annals of Glaciology* **23**: 160–166.
- Van den Broeke MR, Duynkerke PG, Oerlemans J. 1994. The observed katabatic flow at the edge of the Greenland ice sheet during GIMEX-91. *Global and Planetary Change* **9**: 3–15.
- Van den Broeke MR, Smeets CJPP, Ettema J, Kuipers-Munneke P. 2008a. Surface radiation balance in the ablation zone of the west Greenland ice sheet. *Journal of Geophysical Research* **113**: D13105, DOI:10.1029/2007JD009283.
- Van den Broeke MR, Smeets CJPP, Ettema J, van der Veen C, van de Wal RSW, Oerlemans J. 2008b. Partitioning of energy and meltwater fluxes in the ablation zone of the west Greenland ice sheet. *Cryosphere Discussions* **2**: 711–736.
- Van den Broeke MR, van As D, Reijmer CH, van de Wal RSW. 2004. Assessing and improving the quality of unattended radiation observations in Antarctica. *Journal of Atmospheric and Oceanic Technology* **21**(9): 1417–1431.
- Van den Broeke MR, van As D, Reijmer CH, van de Wal RSW. 2005. Sensible heat exchange at the Antarctic snow surface: a study with automatic weather stations. *International Journal of Climatology* **25**: 1080–1101.
- Van den Broeke MR, van Lipzig NPM, van Meijgaard E. 2002. Momentum budget of the East-Antarctic atmospheric boundary layer: results of a regional climate model. *Journal of the Atmospheric Sciences* **59**: 3117–3129.
- Van de Wal RSW, Oerlemans J. 1997. Modelling the short-term response of the Greenland ice sheet to global warming. *Climate Dynamics* **13**: 733–744.
- Wiscombe WJ, Warren SG. 1980. A model for the spectral albedo of snow: I: pure snow. *Journal of the Atmospheric Sciences* **37**: 2712–2733.